# On-Chip Sub-Picometer Continuous Wavelength Fiber-Bragg-Grating Interrogator

Yuan ZHUANG[1], Jun ZOU[2], Jiqiang ZHANG[1], Lu ZHANG[1], Jiahe ZHANG[1], Leixin MENG[1], and Qing YANG[1,3*]

[1]*Research Center for Humanoid Sensing, Zhejiang Lab, Hangzhou 311121, China*

[2]*ZJU-Hangzhou Global Scientific and Technological Innovation Center, Hangzhou 310014, China*

[3]*State Key Laboratory of Modern Optical Instrumentation, College of Optical Science and Engineering, International Research Center for Advanced Photonics, Zhejiang University, Hangzhou 310058, China*

[*]Corresponding author: Qing YANG E-mail: qingyang@zju.edu.cn

**Abstract:** Miniaturized fiber-Bragg-grating (FBG) interrogators are of interest for applications in the areas where weight and size controlling is important, e.g., airplanes and aerospace or in-situ monitoring. An ultra-compact high-precision on-chip interrogator is proposed based on a tailored arrayed waveguide grating (AWG) on a silicon-on-insulator (SOI) platform. The on-chip interrogator enables continuous wavelength interrogation from 1 544 nm to 1 568 nm with the wavelength accuracy of less than 1 pm [the root-mean-square error (RMSE) is 0.73 pm] over the whole wavelength range. The chip loss is less than 5 dB. The $1 \times 16$ AWG is optimized to achieve a large bandwidth and a low noise level at each channel, and the FBG reflection peaks can be detected by multiple output channels of the AWG. The fabricated AWG is utilized to interrogate FBG sensors through the center of gravity (CoG) algorithm. The validation of an on-chip FBG interrogator that works with sub-picometer wavelength accuracy in a broad wavelength range shows large potential for applications in miniaturized fiber optic sensing systems.

**Keywords:** Fiber optic sensing; on-chip interrogator; arrayed waveguide grating; center of gravity

Citation: Yuan ZHUANG, Jun ZOU, Jiqiang ZHANG, Lu ZHANG, Jiahe ZHANG, Leixin MENG, *et al.*, "On-Chip Sub-Picometer Continuous Wavelength Fiber-Bragg-Grating Interrogator," *Photonic Sensors*, 2024, 14(1): 240126.

## 1. Introduction

The fiber-Bragg-grating (FBG) method is one of the well-known optical fiber sensing methods for strain and temperature measurement, which has the characteristics of the small size, immunity to electromagnetic interference, corrosion resistance, and high reliability. FBG sensors have been widely used for structural health monitoring [1], energy security [2, 3], aerospace [4], robots, and medical devices [5–7]. The FBG interrogator is a device that analyzes the data of the FBG by monitoring the central wavelength change. Several approaches for FBG interrogation have been reported in the literature, such as the scanning Fabry-Pérot (FP) cavity [8, 9], tunable lasers [10, 11], and volume phase grating-based spectrometers [12, 13]. However, most traditional interrogators usually suffer from the high price and bulky volume, which limits their applications in some emerging fields, such as unmanned aerial vehicle (UAV) monitoring, lithium-ion battery status monitoring [14], and in-situ three-dimensional (3D) shape sensing [15–18]. On-chip FBG interrogators based on the

Received: 18 November 2022 / Revised: 6 June 2023

DOI: 10.1007/s13320-023-0694-9
Article type: Regular

photonic integrated circuit (PIC) technology have been extensively studied recently due to its advantages of the small size and low power consumption.

According to the employed architectures, the structures of on-chip FBG interrogators can be mainly categorized into four types, including the Mach-Zehnder interferometer (MZI) [19–22], micro-ring resonator (MRR) [23–26], arrayed waveguide grating (AWG) [27–35], and tunable semiconductor laser [36]. Among them, the wavelength accuracy, wavelength range, size of interrogator, and number of FBG sensors are difficult to be satisfied simultaneously. For example, the MZI architecture-based FBG interrogator has high wavelength accuracy, but only a limited number of FBG sensors can be interrogated. The interrogators based on the micro-ring resonator (MRR) architecture can be very small; however, the wavelength range and wavelength accuracy are limited. The tunable semiconductor laser architecture has the advantage of high accuracy, while the wavelength range is limited by the gain range of the laser.

On-chip FBG interrogators based on the tailored AWG are promising to achieve the high wavelength accuracy, large wavelength range, compact size, and multi-sensors interrogated, simultaneously. However, until now, the absolute wavelength accuracy of AWG-based on-chip interrogators is still worse than that of the traditional interrogators with the bulky volume. In this paper, we propose a novel on-chip FBG interrogator with high wavelength accuracy continuously working in a broad measurement range. Thanks to the optimized layout design of the AWG, we successfully fabricated a $1 \times 16$ tailored AWG with the chip loss less than 5 dB and the low noise level of –27 dB. Using the tailored AWG to interrogate the FBG sensor, we are able to achieve the comparable high absolute wavelength accuracy [the root-mean-square error (RMSE) is 0.73 pm] in a large measurement range (24 nm). This paper validates an on-chip FBG interrogator that works with sub-picometer absolute wavelength accuracy.

## 2. Methods

### 2.1 Principle

The proposed on-chip interrogator is based on a tailored AWG. A typical AWG is composed of two free propagation regions (FPR1 and FPR2) connecting each together by an array of waveguides [see Fig. 1(a)]. Different from the conventional AWG designed for wavelength division multiplexing based communication applications where the low adjacent channel crosstalk (an adequate bandwidth) is preferred, the AWG proposed in this paper has an intentionally large bandwidth at each channel, which allows the FBG peak to produce a measurable output signal in multiple AWG channels. The channel bandwidth of the AWG can be calculated by the overlap of the input field profile and mode profile of the output waveguide at the image plane, and determined by the input and output waveguide mode diameter and the pitch between output waveguides [37]. Hence, in order to obtain a desired crosstalk between AWG output channels, we, on one hand, reduce the pitch between adjacent output waveguides, and on the other hand, increase the entrance width of the input waveguide at the object plane. Based on the principle of the center of gravity (CoG) algorithm and according to the measured optical power $P_i$ ($\lambda_{\mathrm{FBG}}$) and the central wavelength $\lambda_i$ at the $i$th output channel of AWG, the peak wavelength $\lambda_{\mathrm{FBG}}$ of the FBG can be derived using the following equation:

$$\lambda_{\mathrm{FBG}} = \frac{\sum P_i(\lambda_{\mathrm{FBG}})\lambda_i}{\sum P_i(\lambda_{\mathrm{FBG}})}. \tag{1}$$

Figure 1(b) also shows the schematic diagram of deriving $\lambda_{\mathrm{FBG}}$ using the tailored AWG. Due to fabrication imperfections, such as the waveguide thickness and width fluctuation, the real transmission spectrum of the designed AWG is slightly different from the ideal Gaussian function, which causes deviations between the calculated

FBG wavelength using the CoG algorithm and the actual FBG central wavelength. Hence, the absolute wavelength accuracy is decreased. In order to tackle this issue, we perform the polynomial curve fitting combined with the sum of the sine curve fitting based on the testing data to improve the absolute wavelength accuracy of the on-chip FBG interrogator.

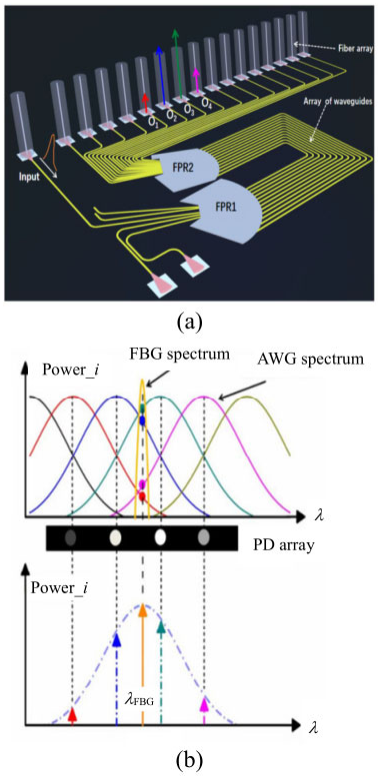


Fig. 1 Principle of the on-chip FBG interrogator: (a) schematic diagram of the proposed AWG and (b) energy of the FBG peak is distributed into multiple channels of AWG and the peak wavelength is derived by the CoG algorithm (PD array stands for photodetector array).

### 2.2 AWG design

A $1\times16$ AWG with the output wavelength spacing $\Delta\lambda = 1.6$ nm is designed on a standard silicon-on-insulator (SOI) wafer with the top silicon layer thickness of 220 nm. As mentioned in the previous section, we reduce the pitch $d_o$ between the adjacent output waveguides and increase the entrance width $w_i$ of the input waveguide to achieve a large bandwidth at each channel. Considering the facts that $d_o$ cannot be reduced indefinitely due to the fabrication requirement and the extra mode mismatch loss between input and output waveguides, which increases with the width of the input waveguide, in order to have a good tradeoff, we set $d_o = 1.2$ μm and $w_i = 5$ μm. In order to reduce the coupling between the adjacent output waveguides, a deeply etched linear taper waveguide with the entrance width of 0.8 μm and exit width of 0.43 μm is introduced between each output waveguide and FPR2. According to our previous research [38], the performance of the AWG is directly related to the footprint of the phase region consisting of FPR1 (FPR2) and array waveguides, which is determined by the radius $R$ of FPR1 (FPR2). Based on (1), $R$ can be derived as

$$R = d_o d_a \frac{\lambda_0}{\Delta\lambda}\cdot\frac{n_a}{n_{ga}\Delta L + n_{gs} d_a \sin\theta_i} \tag{2}$$

where $n_{gs}$ and $n_{ga}$ are the group indices of FPR1 (FPR2) and the array waveguide, respectively. $d_a$ is the pitch between adjacent array waveguides, $\lambda_0$ is the designed central wavelength, and $\Delta\lambda$ is the output wavelength spacing. Usually, $n_{gs}d_a\sin\theta_i << n_{ga}\Delta L$, and hence, $R$ is mainly proportional to the product of $d_o d_a$ for the given $\Delta\lambda$, indicating that $d_o$ and $d_a$ should be appropriately chosen to decrease $R$.

In addition, in order to reduce the sensitivity of the effective index to width fluctuation originating from fabrication imperfections, each waveguide in the phased array is composed of the broad straight waveguide with the width of 800 nm, the narrow single-mode bending waveguide with the width of 430 nm, and adiabatic tapers with the length of 5 μm to connect the broad and narrow waveguides. At the same time, the two FPRs (FPR1 and FPR2) are parallelly arranged with a tilt angle to eliminate the phase error resulting from the effective index difference between curved and straight waveguides. A mode converter based on a shallowly etched multimode interference coupler with the width of 2.3 μm and the length of 2.7 μm connecting to a parabolic taper with the length of 3.5 μm is inserted between the FPR1 (FPR2) and array waveguide to reduce the mode transition loss from the FPR1

(FPR2) to the phased array. Using 3D-finite difference time domain (3D-FDTD) simulation, we obtain that the mode conversion loss is as small as 0.32 dB at the wavelength range of 1 500 nm to 1 600 nm between the FPR1 (FPR2) and array waveguide. Table 1 summarizes the main design parameters of the 1 × 16 AWG. The free spectral range (FSR) is 29.569 nm, which means that 87% of the FSR is occupied in the micro-interrogator design. The footprint of the designed micro-interrogator including all input and output waveguides is only $0.5 \times 2.0$ mm$^2$.

Table 1 Main design parameters of the 1 × 16 AWG.

| Parameter | Quantity |
|---|---|
| Central wavelength (nm) | 1 560.00 |
| Diffraction order | 36 |
| Free spectral range (FSR) (nm) | 29.569 |
| Radius of FPR (μm) | 99.9 |
| Delay length $\Delta L$ (μm) | 20.948 |
| Number of arrayed waveguides | 31 |
| Pitch $d_o$ between adjacent output waveguides (μm) | 1.2 |
| Exit (entrance) width $w_i$ ($w_o$) of input (output) waveguide on the Rowland circle (μm) | 5 (0.8) |
| Footprint of phase region (μm$^2$) | 320 × 410 |

## 2.3 Fabrication and characterization

The proposed on-chip interrogator is fabricated on a 200-mm silicon on insulator (SOI) wafer with the 220-nm thick top silicon layer and 2-μm thick buried oxide layer (BOX). The patterns are defined using 193 nm photolithography and a double etch process. First, the interrogator is defined into a layer of photo-resist (PR) and transferred into the $SiO_2$ hard mask by means of inductively coupled plasma etching. Then, a shallow 70-nm etch is used to define the grating couplers and shallowly-etched multimode interference coupler (MMI) based mode converters, followed by the 150-nm etch to form channel waveguides. At last, an upper-cladding layer of $SiO_2$ with the thickness of 2 μm is deposited by using the plasma enhanced chemical vapor deposition (PECVD). Optical microscope images of the fabricated interrogator are shown in Fig. 2(a).

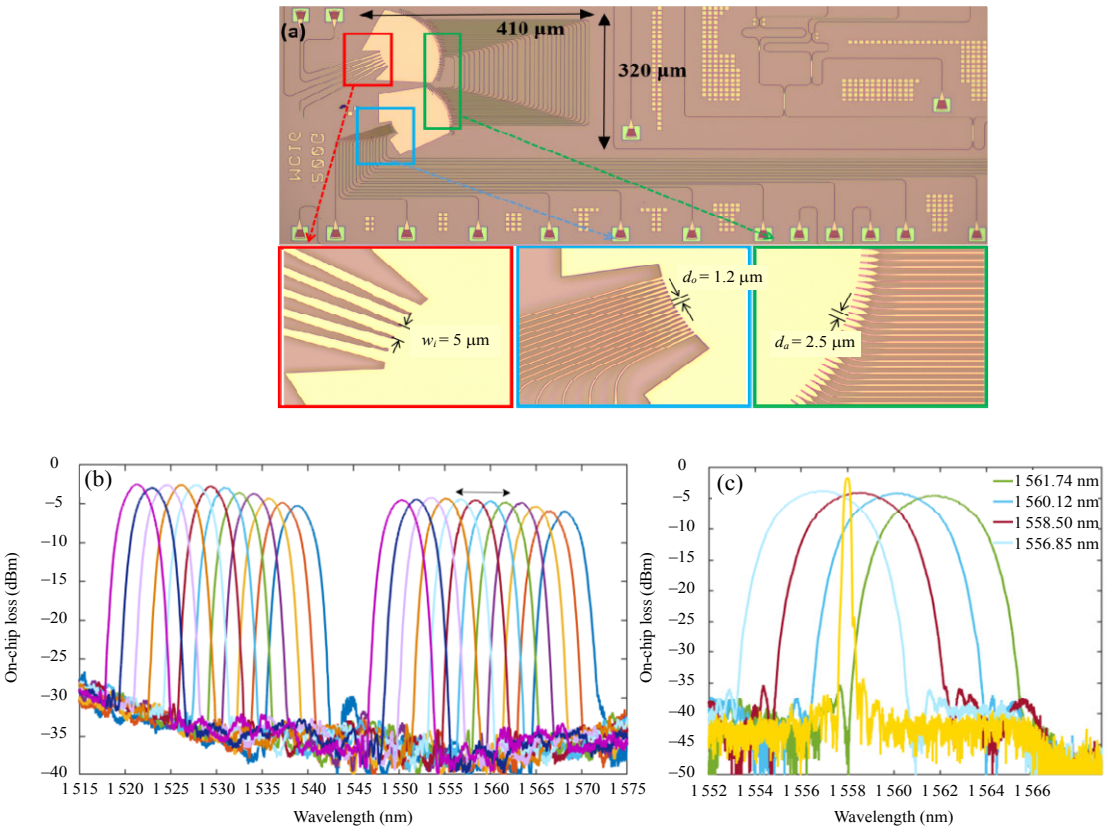


Fig. 2 Characterization of the fabricated on-chip interrogator: (a) microscopic image of the fabricated 1×16 AWG, (b) full spectra of AWG output ports (due to limitations of the test system, only 12 of the 16 channels are tested and shown), and (c) spectral response of 4 AWG channels used for FBG interrogation (The central wavelengths of 4 AWG channels are 1 556.85 nm, 1 558.50 nm, 1 560.12 nm, 1 561.74 nm, respectively, and the central wavelength of FBG is 1 558.00 nm at room temperature.).

Light from a tunable laser source (Agilent, 81608A) firstly passes through a fiber polarization controller, which tunes the polarization direction of the input light to the transverse electric (TE) polarization and then is coupled into the input port of the AWG interrogator via a grating coupler. After propagating through the AWG, the light is coupled out using an array of grating couplers. In order to facilitate the testing, the input/output grating couplers are designed with the 127-μm pitch on the same side for coupling to the $1 \times 18$ fiber arrays, which are directly connected to a multi-channel optical power meter (Agilent, N7744C). By scanning the wavelength of the tunable laser from 1 500 nm to 1 600 nm, the optical power at each output port is collected to obtain the spectral response of the AWG, as shown in Fig. 2(b), where the spectral responses of two diffraction orders are given. Figure 2(c) shows the spectral response of 4 AWG channels used for FBG interrogation, as included in the black double arrow in Fig. 2(b). It is known that the noise level at each channel is below –27 dB due to the optimized layout design of the phase region in the current AWG design. The on-chip loss varies from –6 dB to –4.3 dB.

### 2.4 Experimental set-up

The experimental set-up used to characterize the on-chip FBG interrogator is shown in Fig. 3(a). Broadband light emitted from a super luminescent diode (central wavelength = 1 550 nm and 3-dB bandwidth = 50 nm) is coupled to the FBG sensor through an optical circulator. The FBG sensor under test is written by the femtosecond laser and mounted on a heating platform. Light reflected from the FBG sensor is transmitted through the optical circulator again and split into two equal parts. One is coupled to a commercial interrogator as a reference, and the other is coupled to the on-chip FBG interrogator. Output power at all output channels of the AWG is simultaneously detected by the multi-channel optical power meter, which converts the detected optical power into electrical signals. Finally, the obtained electrical signals are employed to derive the central wavelength of the FBG reflection peak using the CoG algorithm. The on-chip FBG interrogator is mounted on a thermal electric cooler (TEC) to stabilize the operating temperature to eliminate the ambient temperature change induced wavelength shift of the AWG spectral response during the measurement [see Fig. 3(c)]. The absolute wavelength accuracy of the on-chip interrogator is analyzed through comparing the FBG wavelength (FBG-w) recorded by the commercial interrogator and by our packaged miniature interrogator [see Fig. 3(d)].

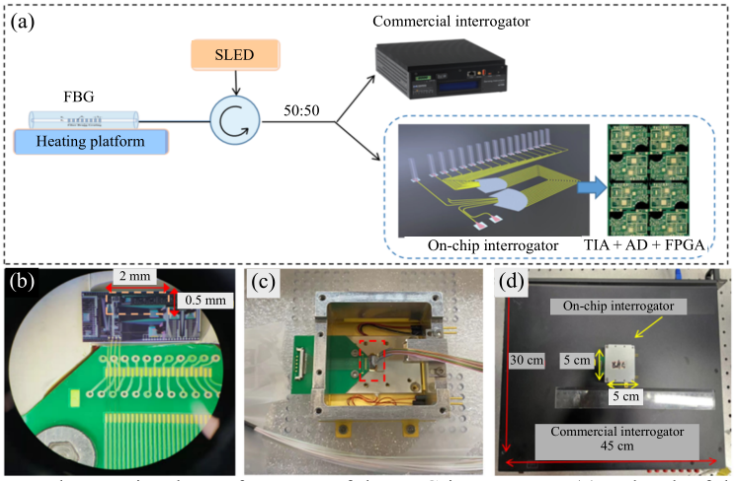


Fig. 3 Experimental set-up to characterize the performance of the FBG interrogator: (a) a sketch of the experimental set-up (SLED is a super luminescent diode, TIA is a trans-impedance amplifier, AD is an analog-to-digital converter, and FPGA is a field programmable gate array), (b) microscope picture of the interrogator chip, (c) interrogator chip mounted on a TEC, and (d) size comparison of packaged on-chip interrogator and commercial interrogator.

## 3. Results and discussion

### 3.1 Single FBG interrogation based on CoG algorithm

In order to evaluate the performance of the proposed on-chip FBG interrogator, the following simulation and experiment are carried out. The central wavelength and 3-dB bandwidth of the FBG sensor at room temperature are 1 558.0 nm and 0.24 nm. The central wavelength of the FBG reflection spectrum varies by controlling the temperature of the FBG sensor. The central wavelengths of the 4 employed AWG channels are 1 556.85 nm, 1 558.50 nm, 1 560.12 nm, and 1 561.74 nm, respectively [see Fig. 2(c)].

First, we theoretically analyze the wavelength accuracy of the fabricated on-chip interrogator based on the measured spectral responses of the AWG and FBG. The AWG spectra and FBG spectra as shown in Fig. 2(c) are imported to the commercial software OptiSystem 13.0. A white light source is used as the broadband light source in the simulation. By tuning the central wavelength of the FBG from 1 558.50 nm to 1 560.10 nm, the CoG wavelength (CoG-w) is derived through the detected power from the 4 AWG output channels [see Fig. 4(a)] using (1). The relationship between the calculated CoG wavelength denoted as CoG-w and the real FBG wavelength denoted as FBG-w is shown in Fig. 4(b) with the black cross marker. It is known that the CoG-w differs slightly from the FBG-w, which can be attributed to the facts that the actual spectral response of the AWG is not perfect due to imperfect fabrications and the CoG algorithm gives exact results only if all the AWG channels have exactly the same spectral shape and constant channel spacing. A "correction" function applying a polynomial curve fitting between CoG-w and FBG-w is also given in Fig. 4(b) with the sky-blue line. Using the "correction" function, we can obtain the "corrected" FBG-w. The wavelength deviation of FBG-w and "corrected" FBG-w can be represented with a "sum of sine" function fitting as shown in Fig. 4(b) with the red line. The absolute wavelength accuracy of the on-chip interrogator is evaluated as the error of "sum of sine" function fitting as shown in Fig. 4(c) with the black stem. It is known that the root mean square error (RMSE) of the absolute wavelength accuracy of 0.31 pm is successfully achieved over the whole wavelength range.

Then, the following experiment has been carried out to validate this on-chip interrogator. A controlled temperature is applied to the FBG sensor under test by means of a heating platform, and the detected power at AWG output channels is recorded by the multi-channel optical power meter. At the same time, the wavelength of the FBG peak is measured using the commercial interrogator. By changing the temperature of the FBG from 70 ℃ to 180 ℃, the central wavelength of the FBG shifts from 1 558.50 nm to 1 560.10 nm and is recorded as the FBG-w by the commercial interrogator. The CoG-w is also calculated based on the detected power from the multi-channel optical power meter as shown in Fig. 4(d). The relationship between the calculated CoG-w and FBG-w is shown in Fig. 4(e). Using the same data processing method, the polynomial curve fitting and the sum of the sine function fitting to the experimental data are performed as shown in Fig. 4(e), respectively. One can see from Fig. 4(f) that the absolute wavelength accuracy is less than 1 pm (RMSE = 0.73 pm) over the whole wavelength range. The difference between the simulated and experimental results can be attributed to the fact that the heating speed of the FBG is so fast, especially between 70 ℃ and 110 ℃ corresponding to the central wavelength changing from 1 558.50 nm to 1 559.08 nm, so that the data acquisitions of the commercial interrogator and multi-channel power meter are not fully synchronous.

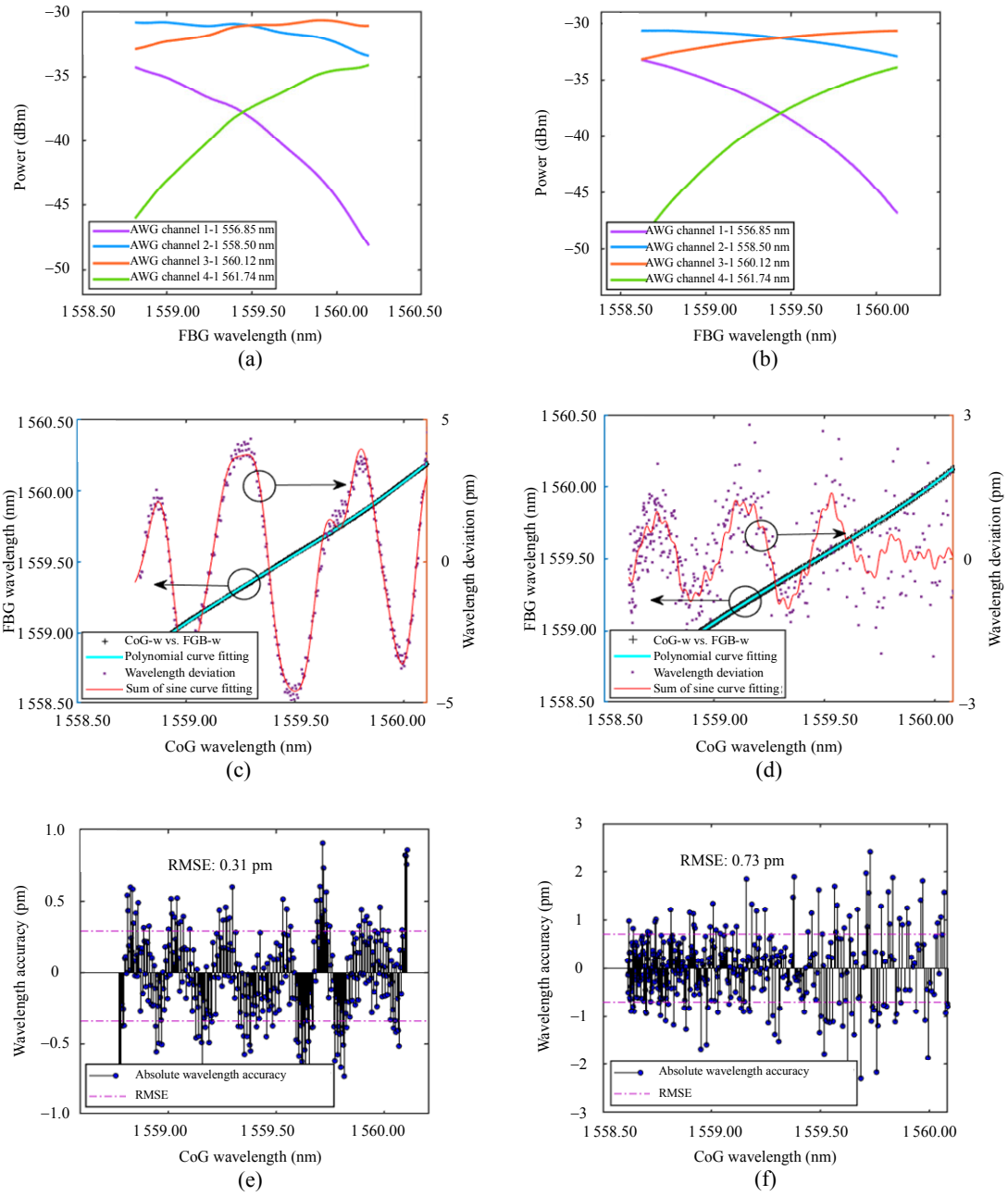


Fig. 4 Simulated and experimental performance of the FBG interrogator: (a) and (b) simulated results and experiment results: detected power from the 4 AWG output channels; (c) and (d) simulated results and experimental results: the relationship of FBG-w and CoG-w (black cross), the "correction" function between CoG-w and FBG-w using the polynomial curve fitting (sky blue line), the wavelength deviation of FBG-w and "corrected" FBG-w (purple dot), and the "sum of sine" function fitting (red line); (e) and (f) simulated results and experimental results: the absolute wavelength accuracy of the on-chip interrogator (black stem).

### 3.2 Continuous wavelength interrogation based on CoG algorithm

Subsequently, we extend the operating wavelength range of the FBG to validate the ability of continuous interrogation of the fabricated interrogator. Since 4 AWG channels in the proposed interrogator are employed to the interrogate single FBG with the dynamic range of 1.6 nm, which is equal to the AWG channel spacing. If we

dynamically select 4 adjacent channels of the 16 channels of the AWG, it is possible to achieve the continuous wavelength interrogation for one FBG sensor across the whole AWG spectrum range. We analyze the performance of 9.60 nm continuous wavelength interrogation between 1 551.80 nm and 1 561.40 nm as shown in Fig. 5(a) where 9 AWG channels are utilized to realize 6 different groups of wavelength interrogation represented by different colors and each group consists of 4 consecutive AWG channels. Figure 5(b) shows the relationship of FBG-w and CoG-w in each group. Using the same "correction" function of the polynomial curve fitting as in Fig. 4, we get the wavelength deviation of FBG-w and "corrected" FBG-w as shown in Fig. 5(c). The difference in the deviation of each group stems from the fact that the spectral shapes of AWG channels are slightly different from each other. Then, the deviation is calibrated using the sum of the sine curve fitting. The calibration results are employed to estimate the absolute wavelength accuracy as shown in Fig. 5(d). The achieved absolute wavelength accuracy is less than 1 pm over the whole wavelength range.

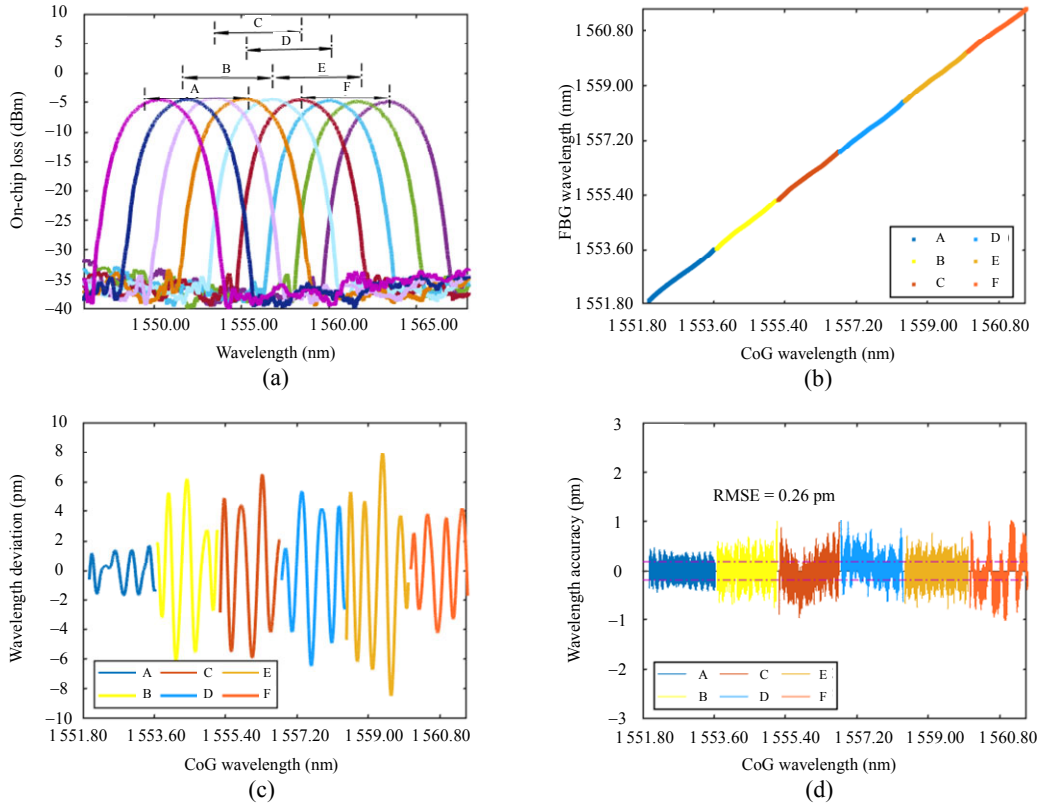


Fig. 5 Continuous wavelength interrogation: (a) schematic diagram of continuous wavelength interrogation based on the CoG algorithm, (b) relationship of FBG-w and CoG-w of 6 groups (A, B, C, D, E, and F) between 1 551.80 nm and 1 561.40 nm, (c) error analysis of the wavelength calibration using the polynomial curve fitting and the sum of the sine curve fitting, and (d) absolute wavelength accuracy of 6 groups applying continuous wavelength interrogation.

### 3.3 Multiple FBGs interrogation

Here, we demonstrate the ability of the on-chip interrogator to simultaneously interrogate multiple FBGs. Due to the limited number of output channels of the fabricated AWG, we use two FBGs as an example. Each FBG is assigned with 4 AWG channels in the experiment. In order to differentiate from the FBG sensor used in Subsection 3.1, the peak wavelengths of these two FBGs are around 1 528 nm and 1 534 nm at room temperature, respectively, as shown in Fig. 6(a), and the spectral response of the AWG working at another diffraction order is also given. When the wavelength difference

of adjacent FBG sensors is less than the dynamic wavelength range, the interference between two sensors will cause errors and affect the accuracy. So, there is a minimum wavelength interval of FBGs, and we must ensure the wavelength difference of FBGs is larger than the minimum wavelength interval. In our design, the minimum wavelength interval of FBGs is 4.8 nm. By controlling the working temperature of these two FBGs, the central wavelength of the FBG1 in Group1 changes from 1 528.30 nm to 1 529.60 nm, while the central wavelength of the FBG2 in Group2 varies from 1 534.40 nm to 1 535.90 nm. The same data processing and analysis as introduced in subsection 3.1 are conducted. It is known from Figs. 6(b)–6(c) that the absolute wavelength accuracy is less than 1 pm for both FBG sensors, agreeing well with that achieved in Subsection 3.1.

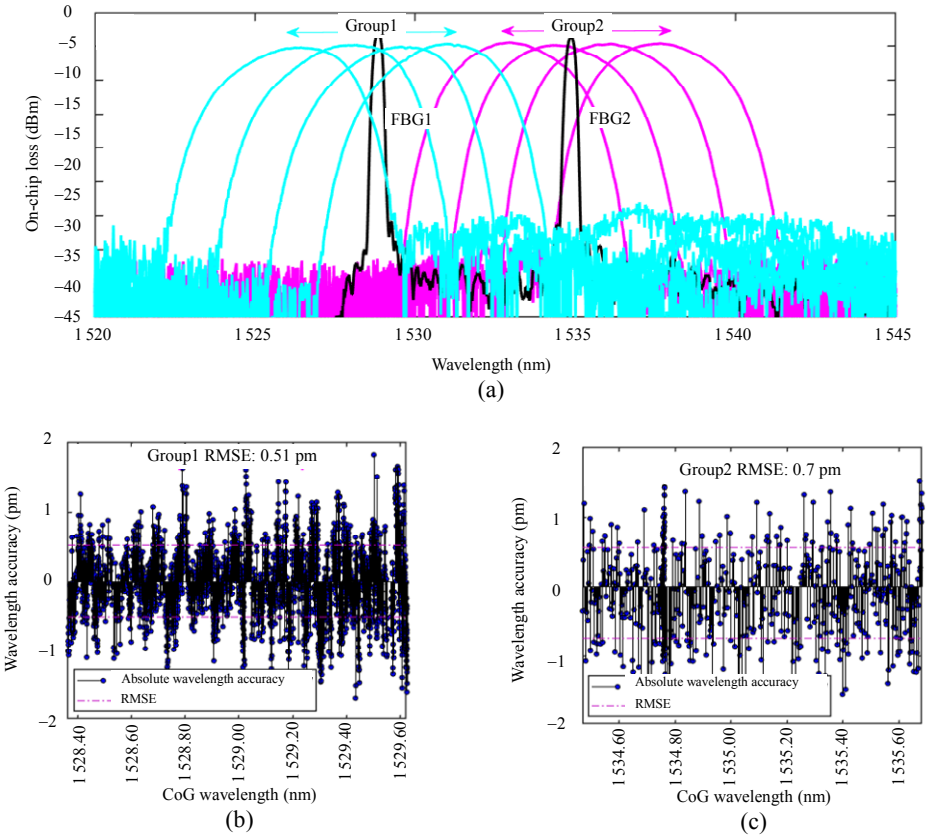


Fig. 6 Simultaneous interrogation of two FBGs: (a) measured spectral response of FBG sensors (FBG1 and FBG2) and two group AWG channels (Group1 and Group2), (b) absolute wavelength accuracy of Group1 (black stem), and (c) absolute wavelength accuracy of Group2 (black stem).

The performance of on-chip FBG interrogators is summarized in Table 2. Compared with the previous reports, it can be seen that our interrogator is the only one that provides the sub-picometer wavelength accuracy in a large wavelength range. Furthermore, it enables continuous wavelength interrogation and also works for multiple FBG sensors. Thanks to the optimized waveguide design of the AWG, the chip loss is less than 5 dB. The ultra-compact high precision interrogator provides a very promising approach for the miniaturized fiber optic sensing system, such as aerospace, unmanned aerial vehicle monitoring, lithium-ion battery status monitoring, and 3D shape sensing in robot and medical fields.

Table 2 On-chip FBG interrogators.

| Authors | Wavelength accuracy (pm) | Wavelength range (nm) | Continuous interrogation | Chip loss (dBm) | Dimension (mm) | Process platform |
|---|---|---|---|---|---|---|
| A. EDGAR *et al*. (2011) [29] | 5 | 50 | No | NA | 50 × 18.5 | $SiO_2$ |
| H.-M. MOON *et al*. (2019) [27] | 7 | 38 | No | NA | NA | $SiO_2$ |
| J. MEYER *et al*. (2019) [14] | 75.9 | 2 | No | NA | 9.0 × 5.0 | Polymer |
| L. CALETA *et al*. (2014) [31] | 2 | 38.4 | Yes | NA | NA | InP |
| D. PUSTAKHOD *et al*. (2016) [34] | NA | 10 | No | ~6 | 2.5 × 2.5 | InP |
| A. KAŹMIERCZAK *et al*. (2018) [30] | NA | 9.6 | No | NA | 6.0 × 4.0 | InP |
| A. TRITA (2015) *et al*. [28] | 2.5 | 50 | Yes | ~6 | 2.2 × 1.5 | Silicon |
| H. Q. LI (2017) *et al*. [33] | 10 | 5 | No | ~6 | 5.0 × 3.0 | Silicon |
| S. M. WENG (2022) *et al*. [32] | 20.6 | 12 | No | ~6.35 | 0.3 × 0.3 | Silicon |
| Our work (2022) | 0.73 | 24 | Yes | ~4.3 | 2.0 × 0.5 | Silicon |

## 4. Conclusions

In summary, we present an on-chip interrogator based on the specially designed 1 × 16 AWG with the footprint of only 0.5 × 2.0 $mm^2$ on the SOI platform. The AWG is optimized with a large 3-dB bandwidth and low noise level, which enables FBG reflection peaks to be detected by multiple output channels using the CoG algorithm and consecutive curve fitting. To the best of our knowledge, the proposed on-chip interrogator has the highest wavelength accuracy (RMSE = 0.73 pm), compared with all AWG-based on-chip interrogators from previous literature at home and abroad. The on-chip interrogator enables continuous wavelength interrogation from 1 544 nm to 1 568 nm. The proposed on-chip interrogator, having the advantages of high wavelength accuracy, continuous wavelength interrogation, and the ultra-compact size, is very promising for applications in miniaturized fiber optic sensing systems (e.g., electric vehicles, airplanes, and aerospace). In the future work, we intend to increase the number of AWG channels or add the optical switch array on the chip to interrogate more FBG sensors. We will also estimate the sampling speed per channel of the interrogator chip and integrate the broad spectrum light source and photodetector array into the same chip.

## Acknowledgment

This work was supported by the National Natural Science Foundation of China (Grant Nos. 62020106002 and 61735017); Innovation Project of Zhejiang Laboratory (Grant No. 2021MG0AL01); the Youth Foundation of Zhejiang Laboratory (Grant No. 2020MC0AA08); Major Scientific Research Project of Zhejiang Laboratory (Grant No. 2019MC0AD02); National Key Basic Research Program of China (Grant No. 2021YFC2401403).

## Declarations

**Conflict of Interest** Qing Yang is an editorial board member/editor-in-chief for Photonic Sensors and was not involved in the editorial review, or the decision to publish this article. All authors declare that there are no competing interests.



## References

[1] Z. C. Fan, X. Z. Diao, K. J. Hu, Y. Zhang, Z. Y. Huang, Y. B. Kang, *et al.*, "Structural health monitoring of metal-to-glass-ceramics penetration during thermal cycling aging using femto-laser inscribed FBG sensors," *Scientific Reports*, 2020, 10(1): 12330.

[2] L. Albero Blanquer, F. Marchini, J. R. Seitz, N. Daher, F. Bétermier, J. Huang, *et al.*, "Optical sensors for operando stress monitoring in lithium-based batteries containing solid-state or liquid electrolytes," *Nature Communications*, 2022, 13(1): 1153.

[3] J. Huang, S. T. Boles, and J. M. Tarascon, "Sensing as the key to battery lifetime and sustainability," *Nature Sustainability*, 2022, 5(3): 194–204.

[4] D. Keller, D. R. Eagan, G. J. Fochesatto, R. Peterson, H. M. Chan, and A. Parker, "Advantages of fiber Bragg gratings for measuring electric motor loadings in aerospace application," *Review of Scientific Instruments*, 2019, 90(7): 075005.

[5] C. Massaroni, M. Zaltieri, D. Lo Presti, A. Nicolo, D. Tosi, and E. Schena, "Fiber Bragg grating sensors for cardiorespiratory monitoring: a review," *IEEE Sensors Journal*, 2021, 21(13): 14069–14080.

[6] D. Lo Presti, C. Massaroni, C. S. J. Leitao, M. D. Domingues, M. Sypabekova, D. Barrera, *et al.*, "Fiber Bragg gratings for medical applications and future challenges: A review," *IEEE Access*, 2020, 8: 156863–156888.

[7] L. Massari, G. Fransvea, J. D'Abbraccio, M. Filosa, G. Terruso, A. Aliperta, *et al.*, "Functional mimicry of Ruffini receptors with fibre Bragg gratings and deep neural networks enables a bio-inspired large-area tactile-sensitive skin," *Nature Machine Intelligence*, 2022, 4(5): 425–435.

[8] C. Li, Y. Wang, and F. Li, "Highly stable FBG wavelength demodulation system based on F-P etalon with temperature control module," *Infrared and Laser Engineering*, 2017, 46(1): 122002–0122002.

[9] Y. C. Ma, C. J. Wang, Y. H. Yang, S. B. Yan, and J. M. Li, "High resolution and wide scale fiber Bragg grating sensor interrogation system," *Optics & Laser Technology*, 2013, 50: 107–111.

[10] A. Roy, A. L. Chakraborty, and C. K. Jha, "Fiber Bragg grating interrogation using wavelength modulated tunable distributed feedback lasers and a fiber-optic Mach-Zehnder interferometer," *Applied Optics*, 2017, 56(12): 3562–3569.

[11] S. K. Ibrahim, R. Mccue, J. A. O'Dowd, M. Farnan, and D. M. Karabacak, "Demonstration of strain independent temperature measurements using optical PM-FBG sensors for ground testing of satellite panels," in *International Conference on Space Optics*, Chania, 2018, pp. 2625–2639.

[12] H. Kim and M. Song, "Linear FBG interrogation with a wavelength-swept fiber laser and a volume phase grating spectrometer," *International Society for Optics and Photonics*, 2011, 7753: 1175–1178.

[13] Z. Cai, J. Hao, D. Bo, J. Phua, and T. M. Chiam, "Design of a fiber Bragg grating sensor interrogation system using volume phase grating and CCD detection," *Proceedings of SPIE: OFS International Conference on Optical Fiber Sensors*, 2012, 8421: 620–623.

[14] J. Meyer, A. Nedjalkov, E. Pichler, C. Kelb, and W. Schade, "Development of a polymeric arrayed waveguide grating interrogator for fast and precise lithium-ion battery status monitoring," *Batteries-Basel*, 2019, 5(4): 66.

[15] T. T. Lai, P. Cheng, C. L. Yan, C. Li, W. B. Hu, and M. H. Yang, "2D and 3D shape sensing based on 7-core fiber Bragg gratings," *Photonic Sensors*, 2020, 10(1): 306–315.

[16] S. Sefati, C. Gao, I. Iordachita, R. H. Taylor, and M. Armand, "Data-driven shape sensing of a surgical continuum manipulator using an uncalibrated fiber Bragg grating sensor," *IEEE Sensors Journal*, 2021, 21(3): 3066–3076.

[17] Y. Liu, A. Zhou, and L. B. Yuan, "Multifunctional fiber-optic sensor, based on helix structure and fiber Bragg gratings, for shape sensing," *Optics & Laser Technology*, 2021, 143: 107327.

[18] X. Z. Xiao, B. J. Xu, X. Z. Xu, B. Du, Z. Y. Chen, C. L. Fu, *et al.*, "Femtosecond laser auto-positioning direct writing of a multicore fiber Bragg grating array for shape sensing," *Optics Letters*, 2022, 47(4): 758–761.

[19] Y. E. Marin, T. Nannipieri, C. J. Oton, and F. Di Pasquale, "Integrated FBG sensors interrogation using active phase demodulation on a silicon photonic platform," *Journal of Lightwave Technology*, 2017, 35(16): 3374–3379 .

[20] Y. E. Marin, A. Celik, S. Faralli, L. Adelmini, C. Kopp, F. Di Pasquale, *et al.*, "Integrated dynamic wavelength division multiplexed FBG sensor interrogator on a silicon photonic chip," *Journal of Lightwave Technology*, 2019, 37(18): 4770–4775.

[21] Y. Marin, T. Nannipieri, C. J. Oton, and F. D. Pasquale, "Fiber Bragg grating sensor interrogators on chip: challenges and opportunities," in *Optical Fiber Sensors Conference*, Jeju, 2017, pp. 1–4.

[22] B. Ouyang, M. Haverdings, R. Horsten, M. Kruidhof, P. Kat, and J. Caro, "Integrated photonics interferometric interrogator for a ring-resonator ultrasound sensor," *Optics Express*, 2019, 27(16): 23408–23421.

[23] A. Shen, C. Qiu, L. Z. Yang, T. G. Dai, Y. B. Li, H. Yu, *et al.*, "Tunable microring based on-chip interrogator for wavelength-modulated optical sensors," *Optics Communications*, 2015, 340: 116–120.

[24] F. Yang, W. J. Zhang, S. X. Zhao, Q. W. Liu, J. F. Ta, and Z. Y. He, "Miniature interrogator for multiplexed FBG strain sensors based on a thermally tunable microring resonator array," *Optics Express*, 2019, 27(5): 6037–6046.

[25] F. Yang, W. J. Zhang, Q. W. Liu, and Z. Y. He, "Silicon-microring-based interrogator for TDM-FBG sensors enabled by pulse compression," *Optics Letters*, 2020, 45(23): 6402–6405.

[26] F. Yang, W. Zhang, S. Zhao, Q. Liu, and Z. He, "Real-time interrogation of multiplexed FBG strain sensors based on a thermally tunable microring resonator array," in *Optical Fiber Communication Conference*, San Diego, 2019, pp. 1–3.

[27] H. M. Moon, S. C. Kwak, K. Im, J. B. Kim, and S. Kim, "Wavelength interrogation system for quasi-distributed fiber Bragg grating temperature sensors based on a 50-GHz array waveguide grating," *IEEE Sensors Journal*, 2019, 19(7): 2598–2604.

[28] A. Trita, E. Voet, J. Vermeiren, D. Delbeke, P. Dumon, S. Pathak, *et al.*, "Simultaneous interrogation of multiple fiber Bragg grating sensors using an arrayed waveguide grating filter fabricated in SOI platform," *IEEE Photonics Journal*, 2015, 7(6): 1–11.

[29] A. Edgar, M. Yan, E. Cornelia, K. Zongjian, and SUN, "Multi-channel monolithic integrated optic fiber Bragg grating sensor interrogator," *Photonic Sensors*, 2011, 1(3): 281–288.

[30] A. Kaźmierczak, A. Jusza, M. Słowikowski, S. Stopiński, and R. Piramidowicz, "Integrated interrogator circuits for fiber optic sensor network in generic InP photonic integrated circuit technology," *Optical Sensing and Detection*, 2018, 10680: 120–129.

[31] L. Caleta, R. S. Evenblij, and J. A. P. Leijtens, "Space gator: a giant leap for fiber optic sensing," in *International Conference on Space Optics*, Tenerife, 2018, pp. 373–380.

[32] S. M. Weng, P. Yuan, W. Zhuang, D. L. Zhang, F. Luo, and L. Q. Zhu, "SOI-based multi-channel AWG with fiber Bragg grating sensing interrogation system," *Photonics-Basel*, 2021, 8(6): 214.

[33] H. Q. Li, X. D. Ma, B. B. Cui, Y. X. Wang, C. Zhang, J. F. Zhao, *et al.*, "Chip-scale demonstration of hybrid III-V/silicon photonic integration for an FBG interrogator," *Optica*, 2017, 4(7): 692–700.

[34] D. Pustakhod, E. Kleijn, K. Williams, and X. Leijtens, "High-resolution AWG-based fiber Bragg grating interrogator," *Photonics Technology Letters*, 2016, 28(20): 2203–2206.

[35] P. Yuan, S. M. Weng, S. K. Ji, D. L. Zhang, and L. Q. Zhu, "Performance analysis of fiber Bragg grating sensor interrogators based on arrayed waveguide gratings," *Optical Engineering*, 2021, 60(6): 066101.

[36] S. K. Ibrahim, M. Farnan, D. M. Karabacak, and J. M. Singer, "Enabling technologies for fiber optic sensing," *Optical Sensing & Detection IV*, 2016, 9899: 229–243.

[37] M. K. Smit and C. V. Dam, "PHASAR-based WDM-devices: Principles, design and applications," *Selected Topics in Quantum Electronics*, 1996, 2(2): 236–250.

[38] J. Zou, F. Y. Sun, C. H. Wang, M. Zhang, J. N. Wang, T. T. Lang, *et al.*, "Silicon-based arrayed waveguide gratings for WDM and spectroscopic analysis applications," *Optics & Laser Technology*, 2022, 147: 107656.